Spinful Topological Phases in Acoustic Crystals with Projective *PT* Symmetry

Yan Meng[1,*] Shuxin Lin,[1,*] Bin-jie Shi,[2,*] Bin Wei,[3,4] Linyun Yang,[1] Bei Yan,[1] Zhenxiao Zhu,[1]
Xiang Xi,[1] Yin Wang,[2] Yong Ge,[2] Shou-qi Yuan,[2] Jingming Chen,[1] Gui-Geng Liu,[5]
Hong-xiang Sun,[2,6,†] Hongsheng Chen,[7] Yihao Yang,[7,‡] and Zhen Gao[1,§]

[1]*Department of Electrical and Electronic Engineering, Southern University of Science and Technology, Shenzhen 518055, China*
[2]*Research Center of Fluid Machinery Engineering and Technology, School of Physics and Electronics Engineering,
Jiangsu University, Zhenjiang 212013, China*
[3]*SKLSM, Institute of Semiconductors, Chinese Academy of Sciences, Beijing 100083, China*
[4]*Center for Excellence in Topological Quantum Computation, University of Chinese Academy of Sciences, Beijing 100190, China*
[5]*Division of Physics and Applied Physics, School of Physical and Mathematical Sciences,
Nanyang Technological University, 21 Nanyang Link, Singapore 637371, Singapore*
[6]*State Key Laboratory of Acoustics, Institute of Acoustics, Chinese Academy of Sciences, Beijing 100190, China*
[7]*Interdisciplinary Center for Quantum Information, State Key Laboratory of Extreme Photonics and Instrumentation, ZJU-Hangzhou
Global Scientific and Technological Innovation Center, Zhejiang University, Hangzhou 310027, China;
International Joint Innovation Center, The Electromagnetics Academy at Zhejiang University, Zhejiang University, Haining 314400, China;
Key Lab. of Advanced Micro/Nano Electronic Devices & Smart Systems of Zhejiang, Jinhua Institute of Zhejiang University,
Zhejiang University, Jinhua 321099, China;
Shaoxing Institute of Zhejiang University, Zhejiang University, Shaoxing 312000, China*

For the classification of topological phases of matter, an important consideration is whether a system is spinless or spinful, as these two classes have distinct symmetry algebra that gives rise to fundamentally different topological phases. However, only recently has it been realized theoretically that in the presence of gauge symmetry, the algebraic structure of symmetries can be projectively represented, which possibly enables the switch between spinless and spinful topological phases. Here, we report the experimental demonstration of this idea by realizing spinful topological phases in "spinless" acoustic crystals with projective space-time inversion symmetry. In particular, we realize a one-dimensional topologically gapped phase characterized by a $2\mathbb{Z}$ winding number, which features double-degenerate bands in the entire Brillouin zone and two pairs of degenerate topological boundary modes. Our Letter thus overcomes a fundamental constraint on topological phases by spin classes.

The concepts of topology and symmetry have revolutionized many branches of physics, ranging from condensed matter physics [1–4] to cold atoms [5], photonics [6–9], acoustics [10–21], and mechanics [22], as manifested by the classification of topological phases of matter. A fundamental dichotomy for topological classification is whether the studied systems are spinful or spinless. Remarkably, under internal or space group symmetries, these two spin classes can exhibit distinct topological phases. A representative example is the space-time inversion symmetry PT, where time-reversal symmetry (T) and space inversion symmetry (P) are combined together [23,24]. For the spinful class, it satisfies $(PT)^2 = -1$, enforcing double-degenerate bands in the entire Brillouin zone (BZ) [Fig. 1(a)]. The time-reversal symmetry, together with particle-hole symmetry, further gives rise to many intriguing topological phases including one-dimensional (1D) topological superconductors or insulators in class DIII, which feature a pair of doubly degenerate topological boundary states at each end [25–27]. By contrast, for the

spinless class, it satisfies $(PT)^2 = 1$, dictating real nondegenerate band structures [Fig. 1(b)] that further lead to its own unique topological phases, such as real Dirac semimetals [28]. Therefore, the spin class seems to impose fundamental constraints on the possible topological phases that a physical system can realize.

However, recent theoretical advances have remarkably revealed that [29], in the presence of gauge symmetry, the above fundamental limitation can be broken; i.e., it is possible to realize spinful (spinless) topological phases previously unique in spinless (spinful) systems. The underlying mechanism is that, with gauge symmetry, the crystalline symmetries of a system should be projectively represented, which further fundamentally modifies the algebraic structure of the symmetry group. For example, in the presence of gauge symmetry, the algebraic structure of translation symmetry can be protectively represented, which enables novel topological phases beyond the conventional topological classification, such as Möbius insulators with $\mathbb{Z}_2$ topological invariants and Möbius-twisted
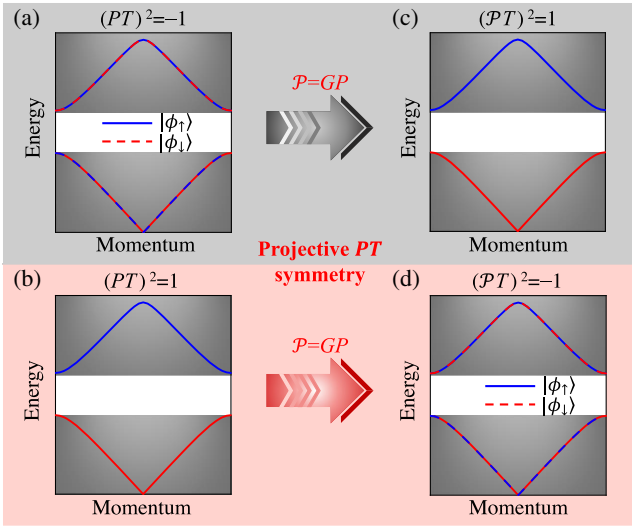
FIG. 1. Switching spinless and spinful topological phases with projective PT symmetry. (a) PT symmetry satisfies $(PT)^2 = -1$ for spinful systems, enabling topological phases with Kramers double-degenerate band structures. (b) PT symmetry satisfies $(PT)^2 = 1$ for spinless systems, enabling topological phases with real nondegenerate band structures. (c),(d) Switching between spinful and spinless phases via projective PT symmetry.

boundary states [30,31]. Another example is that with the gauge symmetry, the space inversion symmetry P will be projectively represented as $\mathcal{P} = GP$ [29,32–34], where G is a gauge transformation. Properly choosing G, the projective PT symmetry (i.e., $\mathcal{P}T$) can satisfy $(\mathcal{P}T)^2 = 1$ [35] for spinful systems [Fig. 1(c)], or satisfy $(\mathcal{P}T)^2 = -1$ for spinless systems [Fig. 1(d)]. This surprisingly suggests that the projective PT symmetry can exchange the fundamental symmetry algebra of spinless and spinful systems, enabling the switching between spinless and spinful topological phases. Note that there exist fundamental differences between the previously reported projective translation symmetry [30,31] and the projective PT symmetry [35] experimentally studied here in underlying symmetries, topological phases, and topological features. First, the phenomenon of band degeneracy originates from different underlying symmetries for these two cases. Second, the projective translation symmetry possesses Möbius insulator phases characterized by a $\mathbb{Z}_2$ topological invariant, while projective PT symmetry guarantees a 1D DIII class topological phase characterized by a $2\mathbb{Z}$ topological invariant. Third, the novel topological phases with projective translation symmetry are featured by the Möbius-twisted edge bands, while the spinful topological phases with projective PT symmetry are featured by the double-degenerate topological boundary modes (Majorana-like Kramers pairs).

Here, we experimentally demonstrate this idea by realizing spinful topological phases in spinless acoustic crystals with projective PT symmetry. Acoustic crystals have hitherto provided a versatile platform to study various topological phases under the framework of quantum-classical analogies [36–47]. Moreover, the positive and negative couplings [48–51] can be easily implemented in acoustic crystals, which are essential to constructing a $\mathbb{Z}_2$ gauge field that can exchange the symmetry algebra between spinless and spinful systems. In particular, we experimentally realize in an acoustic crystal a DIII class 1D topologically gapped phase characterized by a $2\mathbb{Z}$ winding number, an acoustic analog of a 1D T-invariant p-wave topological superconductor [27,52,53]. Such a topological phase features double-degenerate bands and two pairs of degenerate topological boundary modes which were previously unique in spinful systems [54–57]. The former is protected by time-reversal symmetry and termed as Kramers doublet, while the latter is termed as Majorana-like Kramers pairs, which are protected by time-reversal symmetry and effective particle-hole symmetry [23,26]. Moreover, we observe an unconventional topological phase transition and four topological interface states at the domain wall between two nontrivial topological acoustic crystals with opposite nonzero $2\mathbb{Z}$ winding numbers ($\nu = \pm 2$).

To experimentally observe spinful topological phases in a spinless system, we design and fabricate a 1D acoustic crystal, as shown in Fig. 2(a). The experimental sample is fabricated with a standard three-dimensional (3D) stereolithography technique, and the printing material (photosensitive resin) can be considered as hard walls, which enclose a hollow region filled with air. A unit cell of the acoustic crystal is shown in Fig. 2(b), which consists of 8 cylindrical resonators with a height of $h = 20$ mm and a radius of $r_0 = 10$ mm and 20 coupling tubes (with radii of r_1, r_2, r_y, r_{zp}, and r_{zn}). Coupling tubes with positive and negative coupling coefficients are indicated by blue and red colors, respectively. The sign of the coupling coefficients in the acoustic crystals can be determined by the connection positions of the coupling tubes and we adopt bending tubes to realize the negative couplings and straight tubes to realize the positive couplings that exhibit good consistency (see details in Supplemental Material [58]).

The fabricated sample in Fig. 2(a) follows a 1D spinless tight-binding model with positive and negative couplings, as shown in Fig. 2(c). Each unit cell (indicated by a gray cube) has 8 sites (indicated by white spheres). The positive (negative) couplings between nearest-neighbor sites are indicated by blue (red) bonds and labeled as t with different subscripts, where t_y and t_z correspond to the coupling coefficients along y and z directions, respectively; $t_{d,1}$ ($t_{o,1}$) and $t_{d,2}$ ($t_{o,2}$) are the intracell and intercell couplings along the x direction, respectively. The Hamiltonian of the tight-binding model shown in Fig. 2(c) can be written as

$$\mathcal{H} = t_y \Gamma_{100} + t_z \Gamma_{301} + \sum_{\{s=d,o\}} \begin{bmatrix} 0 & u_s \\ u_s^* & 0 \end{bmatrix} \otimes M_s, \quad (1)$$

where $\Gamma_{\mu\nu\lambda}$ is defined as $\Gamma_{\mu\nu\lambda} = \rho_\mu \otimes \tau_\nu \otimes \sigma_\lambda$. ρ_μ, τ_ν, and σ_λ are Pauli matrices and $\mu, \nu, \lambda = 0, 1, 2, 3$. M_s is a
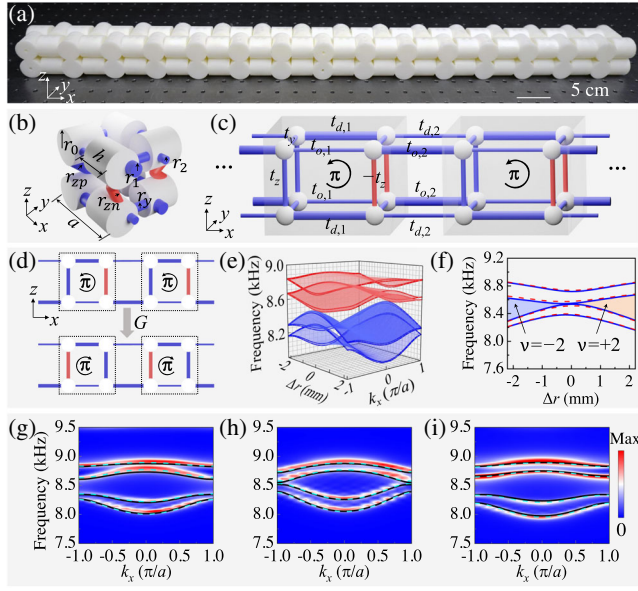
FIG. 2. Experimental demonstration of Kramers double-degenerate band structures. (a) Photograph of the fabricated 1D acoustic crystal sample with 15 unit cells along the x direction. (b) Unit cell of the 1D acoustic crystal with a lattice constant a. Red (blue) tubes represent negative (positive) couplings. (c) Configuration for the tight-binding model of the 1D acoustic crystal. Gray cubes: unit cell of the configuration. White spheres: sites. Blue (red) bonds: positive (negative) couplings. (d) Gauge transformation process (gray arrow) switches the sign of couplings in the z direction, while keeping the synthetic gauge flux π in each plaquette invariant. (e) Phase diagram of the simulated band structures of the 1D acoustic crystal as a function of the wave vector k_x and the radius contrast Δr defined as $\Delta r = (r_1 - r_2)$. (f) Evolution of the middle band gaps and topological winding numbers ($\nu = \pm 2$) as a function of Δr. (g)–(i) Measured (background colors) and simulated (black solid and cyan dashed lines) Kramers doublet of the 1D acoustic crystal with (g) $\Delta r = -2.2$ mm, (h) $\Delta r = 0$ mm, and (i) $\Delta r = 2.2$ mm, respectively. The color scale indicates the measured acoustic energy density.

diagonal matrix. When its subscript "s" is written as "d" or "o", we have $M_d = \mathrm{diag}(1, 0, 0, 1)$ and $M_o = \mathrm{diag}(0, 1, 1, 0)$. The Bloch functions in the Hamiltonian are described as $u_d = t_{d,1} + t_{d,2} e^{-ik}$ and $u_o = t_{o,1} + t_{o,2} e^{-ik}$, respectively. With the Hamiltonian in Eq. (1), we then investigate the projective PT symmetry of the designed configuration with spinless character. In our case, $\hat{T}$ and $\hat{P}$ operators can be defined as $\hat{T} = \hat{\mathcal{K}}$ and $\hat{P} = \Gamma_{111}\hat{I}$, respectively. Both the time-reversal symmetry T and the space inversion symmetry P preserve the spin of the Hamiltonian in Eq. (1); thus the space-time inversion symmetry satisfies $(PT)^2 = 1$ (see details in the Supplemental Material [58]). In particular, the negative and positive couplings in our system can construct a $\mathbb{Z}_2$ gauge field with $\mathbb{Z}_2 = \{\pm 1\}$. In Fig. 2(d), we present the front view (x-z plane) of the tight-binding model. It can be

seen that within each plaquette (indicated by a dashed rectangular box), there are one negative and three positive coupling bonds, and thus encloses a π gauge flux. Gauge transformation (G) on the $\mathbb{Z}_2$ gauge field is defined as $G = \Gamma_{003}$ and satisfies [29,72]

$$[G, T] = 0, \qquad \{G, P\} = 0, \qquad G^2 = 1. \qquad (2)$$

Here, the gauge transformation G only swaps the negative and positive coupling coefficients along the z direction, while keeping other coupling coefficients unchanged. The gauge transformation process is schematically illustrated in Fig. 2(d).

It can be seen that the gauge flux in each plaquette is invariant under the gauge transformation G (see details in the Supplemental Material [58]). In the presence of gauge symmetry, the space inversion symmetry operator P can be projectively represented as $\mathcal{P} = GP$; thus $\mathcal{P}^2 = (GP) * (GP) = -(P)^2 = -1$. Hence, the projective PT symmetry for the system satisfies $(\mathcal{P}T)^2 = -1$ (see details in the Supplemental Material), indicating that the Kramers double-degenerate band structures previously unique to spinful systems are realizable in a spinless system under projective PT symmetry. Two pseudospins can be defined as $\psi_+ = U\psi_1$ and $\psi_- = U\psi_2$, where ψ_1 and ψ_2 are two eigenstates of the Hamiltonian $\mathcal{H}(k)$ and U is a unitary transformation, $U = e^{(i\pi/4)\Gamma_{100}} e^{-(i\pi/4)\Gamma_{133}}$. When the pseudo time-reversal symmetry is defined as $\mathcal{P}T$, the pseudospin satisfies $\psi_+ \xrightarrow{\mathcal{P}T} \psi_- \xrightarrow{\mathcal{P}T} -\psi_+ \xrightarrow{\mathcal{P}T} -\psi_-$.

Next, we demonstrate the Kramers doublet of the designed 1D acoustic crystal. Here, we set $r_y = 2.2$ mm, $r_{zn} = 2.7$ mm, $r_{zp} = 2.9$ mm, $(r_1 + r_2) = 6.2$ mm, and $(r_1 - r_2) = \Delta r$. To obtain the complete phase diagram, we numerically solve the band structures of the 1D acoustic crystals with a finite element method (commercial software COMSOL MULTIPHYSICS). We sweep Δr from -2.2 to 2.2 mm, and plot the eigenfrequency spectrum as a function of Δr and wave vector k_x in Fig. 2(e). It can be seen that there exist four Kramers double-degenerate bands guaranteed by the projective PT symmetry $(\mathcal{P}T)^2 = -1$, and the targeted band gap closes at $\Delta r = 0$ with a topological phase transition.

The Hamiltonian in Eq. (1) can be decomposed into two off-diagonal blocks on account of its sublattice symmetry S. Therefore, the winding number (ν) for the 1D acoustic crystal can be calculated by one of the two decomposed blocks [29]. In contrast to the conventional Su-Schrieffer-Heeger model, which is characterized by an integer winding number of $\mathbb{Z}$, the designed 1D acoustic crystal is characterized by a winding number restricted to an even integer $\nu = 2\mathbb{Z}$ (see details in the Supplemental Material [58]). This acoustic crystal is classified into the DIII class topological phase because it satisfies $(\hat{\mathcal{P}}\hat{T})^2 = -1$ and $\{\hat{\mathcal{P}}\hat{T}, \hat{S}\} = 0$, where $\hat{S} = \Gamma_{333}\hat{I}$ is a sublattice symmetry

operator. The evolution of frequencies as a function of Δr at the BZ boundary (i.e., frequencies at $k_x = \pm\pi/a$) is shown in Fig. 2(f), which clearly shows the band gap closure at $\Delta r = 0$. Winding numbers for systems with different Δr are shaded by blue ($\nu = -2$) and orange ($\nu = +2$) colors, respectively. It can be seen that the winding number evolves from $\nu = -2$ to $\nu = +2$ as Δr evolves from negative to positive. $\Delta r = 0$ is a critical point for the unconventional topological phase transition that occurs between two nontrivial topological phases with opposite nonzero $2\mathbb{Z}$ winding numbers.

The projective PT symmetry of the proposed 1D acoustic crystals guarantees Kramers double-degenerate band structures for all Δr. To experimentally demonstrate this, we fabricate three samples with different Δr (-2.2, 0, and 2.2 mm, respectively) and apply spatial Fourier transform to the measured complex acoustic pressure distributions from real space to reciprocal space. As shown in Figs. 2(g)–2(i), for each sample, four Kramers double-degenerate bands are observed in the entire BZ, and the measured results (background colors) are in good agreement with the simulated results (black solid and cyan dashed lines).

Then, we explore the Kramers pairs of topological boundary modes supported by the proposed 1D acoustic crystals. Based on the first-principles calculation, the acoustic crystals with $\Delta r \neq 0$ exhibit nontrivial spinful topological phases with nonzero $2\mathbb{Z}$ winding numbers. Kramers pairs of topological boundary modes are guaranteed by the bulk-edge correspondence. To verify the above prediction, we numerically calculate the eigenfrequency spectrum of a finite 1D acoustic crystal (15 unit cells) with $\Delta r = 2.2$ mm (see the tight-binding model analysis in Supplemental Material [58]). As shown in Fig. 3(a), two pairs of topological boundary modes (colored dots) localized at the left or right ends can be observed within the band gap of bulk states (gray squares), which are termed as Kramers pairs of topological boundary modes protected by space-time inversion symmetry (see Supplemental Material), in contrast to recently reported degenerate zero-energy topological states at disclinations, as a result of the preservation of chiral symmetry [73]. The inset in Fig. 3(a) shows the enlarged frequency regime of the four topological boundary modes (see Supplemental Material for detailed explanation on the slight nondegeneracy of four topological boundary modes and the corresponding optimization). The simulated acoustic pressure distributions of the four topological boundary modes are plotted in Fig. 3(b), with each two of them localizing at the same end and forming a Kramers pair. Within each Kramers pair, two topological boundary modes exhibit distinct phase distributions which are indicated by "+" and "−" signs, for instance, in-phase modes at CS1 (CS3) and out-of-phase modes at CS2 (CS4). Moreover, these topological edge states are in principle robust against any kind of disorders or
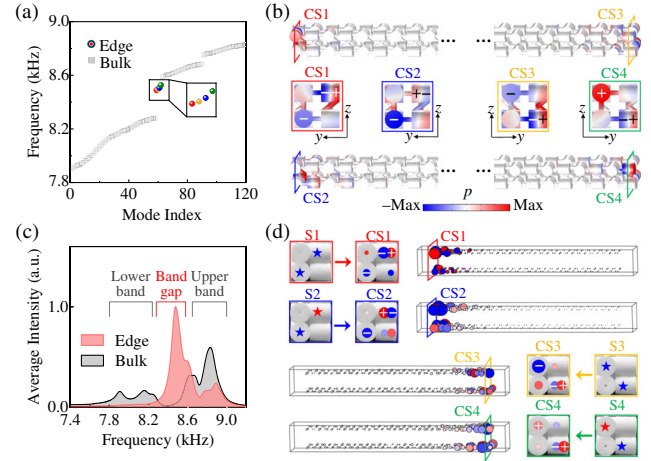

FIG. 3. Observation of Kramers pairs of topological boundary modes. (a) Simulated eigenfrequency spectrum of a finite-size 1D acoustic crystal (15 unit cells); eigenstates can be classified as bulk modes (gray squares) and boundary modes (color dots). Inset: enlarged frequency regime of boundary modes. (b) Simulated acoustic pressure distributions of two pairs of Kramers topological boundary modes. (c) Measured averaged intensity spectra for bulk (gray) and edge (red) regions; the simulated band gap is highlighted by a red frame. (d) Measured acoustic pressure distributions of two pairs of Kramers topological boundary modes. Insets: excitation sources (S1, S2, S3, and S4) and measured acoustic pressure distributions at four cross sections (CS1, CS2, CS3, and CS4). Colored stars indicate the position and phase of the excitation source. Colored circles with "+" and "−" signs indicate the acoustic pressure distributions and symmetry of the excited boundary modes at each cross section.

perturbations that preserve the projective PT symmetry and sublattice symmetry (see detailed numerical studies in Supplemental Material). For acoustic crystal with $\nu = -2$, its simulated Kramers pairs of topological boundary modes are presented in Supplemental Material. Note that the sign of the winding number only affects the acoustic field distributions of the Majorana-like Kramers pairs.

We then experimentally demonstrate the Kramers pairs of topological boundary modes. The sample is artificially divided into two nonoverlapping parts: the "edge" region consists of 8 cylindrical resonators at both ends of the acoustic crystal and the "bulk" region consists of the remaining 112 resonators. The measured results are shown in Fig. 3(c) (see experimental details for measuring the average intensity in Supplemental Material [58]), from which we can observe that within the bulk band gap regime (about 8.3–8.5 kHz), the measured intensity spectrum of the edge region remains much higher than that of the bulk region, indicating the existence of edge states. Moreover, the measured peak frequency ranges of the edge and bulk regions match well with the simulated eigenfrequency spectrum shown in Fig. 3(a). See the measurement methods in Supplemental Material [58].

We also experimentally map the acoustic pressure distributions of the Kramers pairs of topological boundary modes. Using two acoustic point sources (indicated by red or blue stars) with designed phases difference (0 or π) placed at the left or right edges of the 1D acoustic crystal, we selectively excite each pair of topological boundary modes that possess different mode symmetries. Figure 3(d) shows the measured acoustic pressure distributions of the Kramers pairs of topological boundary modes localized on the left or right edges of the 1D acoustic crystal, matching well with the simulated results shown in Fig. 3(b). Moreover, each pair of the measured topological edge states with their acoustic pressure localized on the same edge (left or right) exhibits almost the same eigenfrequency but different phase distributions (indicated by "+" and "−" signs), as shown in CS1 and CS2 (or CS3 and CS4). The experimental observations of Kramers pairs of topological boundary modes together with Kramers double-degenerate band structures, which were previously unique to spinful systems, demonstrate the realization of spinful topological phases in spinless acoustic crystals. For comparison, the simulated average intensity and acoustic pressure distributions of topological edge states excited by a phased source array can be found in Supplemental Material [58].

Finally, we demonstrate the topological interface states between two nontrivial spinful topological phases with

opposite winding numbers ($\nu = \pm 2$). Figure 4(a) shows the fabricated sample, which consists of 8 unit cells with winding number $\nu = -2$ on the left side and 8 unit cells with winding number $\nu = +2$ on the right side, and the red plane indicates the interface. According to the bulk-edge correspondence, the total number of topological interface states should be exactly equal to the difference between the winding numbers of two nontrivial topological acoustic crystals. Indeed, four topological interface states (colored stars) emerge within the bulk (gray squares) band gap of the simulated eigenfrequency spectrum of the sample, as shown in Fig. 4(b). Using the pump and probe method, we measure the average intensity of the "interface" (red color) and "bulk" (gray color) regions, as shown in Fig. 4(c). We observe that the intensity peak of the interface region is located within the bulk band gap, implying the existence of topological interface states. Following a similar procedure used to probe the four topological edge states, we plot the simulated [Fig. 4(d)] and measured [Fig. 4(e)] acoustic pressure distributions of the topological interface states, which are localized in the vicinity of the sample interface and decay exponentially away from it.

In conclusion, we have experimentally realized spinful topological phases in "spinless" acoustic crystals, breaking the fundamental constraint on topological phase classification by the spin class. By introducing negative and positive couplings to engineer an equivalent $\mathbb{Z}_2$ gauge field in acoustic crystals, the projective PT symmetry can completely modify the fundamental symmetry algebra of a system, making an originally spinless system behave like a spinful one. We observe the Kramers double-degenerate band structures and the Kramers pairs of topological boundary modes in acoustic crystals, which were previously unique to spinful systems. Moreover, the double-degenerate topological states not only can act as ideal carriers of acoustic information transport with multiple transmission channels, but also can increase the density of states [73] which may have promising potential applications in phononic lasing [74,75] and sound power emission [76]. Though we choose acoustic crystals as a versatile platform for proof of principles, this protocol is general and can be directly extended to other spinless systems such as photonics, mechanics, and electronic circuits. This paradigm of projective symmetry reveals new perspectives on topological phase classification and opens the door to a vast landscape of unexplored topological physics with gauge degrees of freedom.
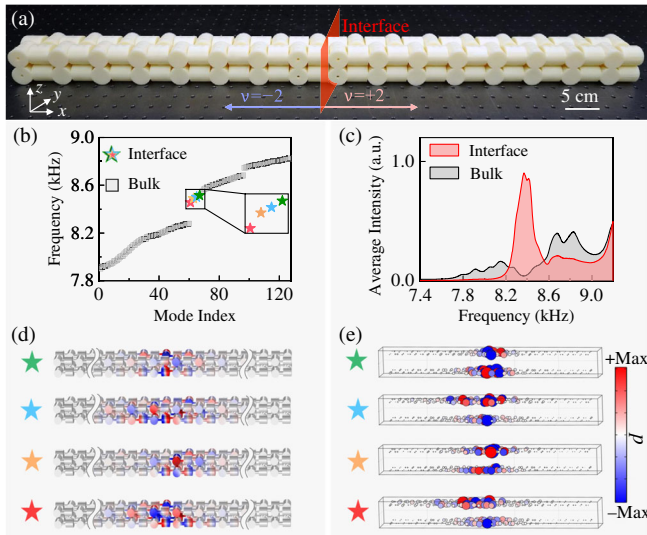

FIG. 4. Topological interface states between two spinful topological acoustic crystals with opposite topological invariants. (a) Photograph of the sample consists of two nontrivial acoustic crystals with opposite nonzero winding numbers $\nu = -2$ on the left side and $\nu = 2$ on the right side, respectively. Red plane represents the interface. (b) Simulated eigenfrequency spectrum for the configuration shown in (a). Inset: enlarged spectral region of four topological interface states (colored stars). (c) Measured average intensity spectra for the "interface region" (red) and "bulk region" (gray), respectively. (d) Simulated and (e) measured acoustic pressure distributions of the four topological interface states.

---

*These authors contributed equally to this work.
†jsdxshx@ujs.edu.cn
‡yangyihao@zju.edu.cn
§gaoz@sustech.edu.cn

[1] K. V. Klitzing, G. Dorda, and M. Pepper, Phys. Rev. Lett. 45, 494 (1980).

[2] Y. B. Zhang, Y. W. Tan, H. L. Stormer, and P. Kim, Nature (London) 438, 201 (2005).

[3] C. L. Kane and E. J. Mele, Phys. Rev. Lett. 95, 146802 (2005).

[4] B. A. Bernevig, T. L. Hughes, and S. C. Zhang, Science 314, 1757 (2006).

[5] N. R. Cooper, J. Dalibard, and I. B. Spielman, Rev. Mod. Phys. 91, 015005 (2019).

[6] Z. Wang, Y. Chong, J. D. Joannopoulos, and M. Soljačić, Nature (London) 461, 772 (2009).

[7] L. Lu, J. D. Joannopoulos, and M. Soljaclc, Nat. Photonics 8, 821 (2014).

[8] L. H. Wu and X. Hu, Phys. Rev. Lett. 114, 223901 (2015).

[9] T. Ozawa, H. M. Price, A. Amo, N. Goldman, M. Hafezi, L. Lu, M. C. Rechtsman, D. Schuster, J. Simon, O. Zilberberg, and I. Carusotto, Rev. Mod. Phys. 91, 015006 (2019).

[10] M. Xiao, G. Ma, Z. Yang, P. Sheng, Z. Q. Zhang, and C. T. Chan, Nat. Phys. 11, 240 (2015).

[11] Z. Yang, F. Gao, X. Shi, X. Lin, Z. Gao, Y. Chong, and B. Zhang, Phys. Rev. Lett. 114, 114301 (2015).

[12] X. Ni, C. He, X. C. Sun, X. P. Liu, M. H. Lu, L. Feng, and Y. F. Chen, New J. Phys. 17, 053016 (2015).

[13] A. B. Khanikaev, R. Fleury, S. H. Mousavi, and A. Alu, Nat. Commun. 6, 8260 (2015).

[14] Y. G. Peng, C. Z. Qin, D. G. Zhao, Y. X. Shen, X. Y. Xu, M. Bao, H. Jia, and X. F. Zhu, Nat. Commun. 7, 13368 (2016).

[15] Z. Zhang, Q. Wei, Y. Cheng, T. Zhang, D. Wu, and X. Liu, Phys. Rev. Lett. 118, 084303 (2017).

[16] C. He, S. Y. Yu, H. Ge, H. Wang, Y. Tian, H. Zhang, X. C. Sun, Y. B. Chen, J. Zhou, M. H. Lu, and Y. F. Chen, Nat. Commun. 9, 4555 (2018).

[17] W. Zhu, X. Fang, D. Li, Y. Sun, Y. Li, Y. Jing, and H. Chen, Phys. Rev. Lett. 121, 124501 (2018).

[18] X. Wen, C. Qiu, Y. Qi, L. Ye, M. Ke, F. Zhang, and Z. Liu, Nat. Phys. 15, 352 (2019).

[19] X. Zhang, H. X. Wang, Z. K. Lin, Y. Tian, B. Xie, M. H. Lu, Y. F. Chen, and J. H. Jiang, Nat. Phys. 15, 582 (2019).

[20] H. Xue, D. Jia, Y. Ge, Y. J. Guan, Q.Wang, S. Q. Yuan, H. X. Sun, Y. D. Chong, and B. Zhang, Phys. Rev. Lett. 127, 214301 (2021).

[21] H. Xue, Y. Yang, and B. Zhang, Nat. Rev. Mater. 7, 974 (2022).

[22] R. Süsstrunk and S. D. Huber, Science 349, 47 (2015).

[23] A. P. Schnyder, S. Ryu, A. Furusaki, and A. W. W. Ludwig, Phys. Rev. B 78, 195125 (2008).

[24] Y. X. Zhao, A. P. Schnyder, and Z. D. Wang, Phys. Rev. Lett. 116, 156402 (2016).

[25] L. Fidkowski and A. Kitaev, Phys. Rev. B 83, 075103 (2011).

[26] C. L. M. Wong and K. T. Law, Phys. Rev. B 86, 184516 (2012).

[27] J. C. Budich and E. Ardonne, Phys. Rev. B 88, 134523 (2013).

[28] Y. X. Zhao and Y. Lu, Phys. Rev. Lett. 118, 056401 (2017).

[29] Y. X. Zhao, C.Chen, X. L. Sheng, and S. A. Yang, Phys. Rev. Lett. 126, 196402 (2021).

[30] H. Xue, Z. Wang, Y. X. Huang, Z. Cheng, L. Yu, Y. X. Foo, Y. X. Zhao, S. A. Yang, and B. Zhang, Phys. Rev. Lett. 128, 116802 (2022).

[31] T. Li, J. Du, Q. Zhang, Y. Li, X. Fan, F. Zhang, and C. Qiu, Phys. Rev. Lett. 128, 116803 (2022).

[32] S. Bieri, C. Lhuillier, and L. Messio, Phys. Rev. B 93, 094437 (2016).

[33] Y. X. Zhao, Y. X. Huang, and S. A. Yang, Phys. Rev. B 102, 161117 (2020).

[34] L. B. Shao, Q. Liu, R. Xiao, S. A. Yang, and Y. X. Zhao, Phys. Rev. Lett. 127, 076401 (2021).

[35] J. Herzog-Arbeitman, Z.-D. Song, N. Regnault, and B. A. Bernevig, Phys. Rev. Lett. 125, 236804 (2020).

[36] R. Fleury, D. L. Sounas, and C. F. Sieck, Science 343, 516 (2014).

[37] C. He, X. Ni, H. Ge, X. C. Sun, Y. B. Chen, M. H. Lu, X. P. Liu, and Y. F. Chen, Nat. Phys. 12, 1124 (2016).

[38] J. Lu, C. Qiu, L. Ye, X. Fan, M. Ke, F. Zhang, and Z. Liu, Nat. Phys. 13, 369 (2017).

[39] J. Lu, C. Qiu, W. Deng, X. Huang, F. Li, F. Zhang, S. Chen, and Z. Liu, Phys. Rev. Lett. 120, 116802 (2018).

[40] F. Li, X. Huang, J. Lu, J. Ma, and Z. Liu, Nat. Phys. 14, 30 (2018).

[41] H. He, C. Qiu, L. Ye, X. Cai, X. Fan, M. Ke, F. Zhang, and Z. Liu, Nature (London) 560, 61 (2018).

[42] X. Ni, M. Weiner, A. Alù, and A. B. Khanikaev, Nat. Mater. 18, 113 (2019).

[43] H. Xue, Y. Yang, F. Gao, Y. Chong, and B. Zhang, Nat. Mater. 18, 108 (2019).

[44] H. Xue, Y. Yang, G. Liu, F. Gao, Y. Chong, and B. Zhang, Phys. Rev. Lett. 122, 244301 (2019).

[45] M. Xiao, L. Ye, C. Qiu, H. He, Z. Liu, and S. Fan, Sci. Adv. 6, eaav2360 (2020).

[46] M. Weiner, X. Ni, M. Li, A. Alù, and A. B. Khanikaev, Sci. Adv. 6, eaay4166 (2020).

[47] C. H. Xia, H. S. Lai, X. C. Sun, C. He, and Y. F. Chen, Phys. Rev. Lett. 128, 115701 (2022).

[48] Y. Qi, C. Qiu, M. Xiao, H. He, M. Ke, and Z. Liu, Phys. Rev. Lett. 124, 206601 (2020).

[49] H. Xue, Y. Ge, H. X. Sun, Q. Wang, D. Jia, Y. J. Guan, S. Q. Yuan, Y. Chong, and B. Zhang, Nat. Commun. 11, 2442 (2020).

[50] X. Ni, M. Li, M. Weiner, A. Alù, and A. B. Khanikaev, Nat. Commun. **11,** 2108 (2020).

[51] Z. Y. Chen, S. A. Yang, and Y. X. Zhao, Nat. Commun. **13,** 2215 (2022).

[52] K. T. Law, P. A. Lee, and T. K. Ng, Phys. Rev. Lett. **103,** 237001 (2009).

[53] X. J. Liu, C. L. Wong, and K. T. Law, Phys. Rev. X **4,** 021018 (2014).

[54] M. J. Klein, Am. J. Phys. **20,** 65 (1952).

[55] A. Yu. Kitaev, Phys. Usp. **44,** 131 (2001).

[56] L. Fu and C. L. Kane, Phys. Rev. Lett. **100,** 096407 (2008).

[57] Z. Su, W. Gao, B. Liu, L. Huang, and Y. Wang, New J. Phys. **24,** 033025 (2022).

[58] See Supplemental Material at http://link.aps.org/supplemental/10.1103/PhysRevLett.130.026101 for (i) the tight-binding model and Hamiltonian of the proposed 1D acoustic system, (ii) the topological classification based on symmetries, (iii) the winding number and Majorana-like zero modes, (iv) the Kramers double-degenerate band structures and topological boundary modes, (v) the mechanism of positive and negative couplings in acoustic crystals, (vi) the explanation on the slight nondegeneracy of the topological boundary modes, (vii) the robustness of the topological boundary modes, (viii) the simulated average intensity spectra of the boundary modes, (ix) the simulated band structure and boundary modes of the acoustic crystal, (x) the topological boundary modes for two connected nontrivial acoustic crystals with opposite nonzero winding numbers, and (xi) the experimental details for measuring average intensity, which includes Refs. [59–71].

[59] J. B. Kogut, Rev. Mod. Phys. **51,** 659 (1979).

[60] M. Xiao, W. J. Chen, W. Y. He, and C. T. Chan, Nat. Phys. **11,** 920 (2015).

[61] S. Mittal, V. V. Orre, G. Zhu, M. A. Gorlach, A. Poddubny, and M. Hafezi, Nat. Photonics **13,** 692 (2019).

[62] R. Keil, C. Poli, M. Heinrich, J. Arkinstall, G. Weihs, H. Schomerus, and A. Szameit, Phys. Rev. Lett. **116,** 213901 (2016).

[63] S. Weinberg, *The Quantum Theory of Fields* (Cambridge University Press, Cambridge, England, 1995).

[64] A. W. Ludwig, Phys. Scr. **T168,** 014001 (2016).

[65] C. Chiu, J. Teo, A. Schnyder, and S. Ryu, Rev. Mod. Phys. **88,** 035005 (2016).

[66] J. He, Y. X. Zhu, Y. J. Wu, L. Liu, Y.Liang, and S. P. Kou, Phys. Rev. B **87,** 075126 (2013).

[67] M. Sato and S. Fujimoto, J. Phys. Soc. Jpn. **85,** 072001 (2016).

[68] Z. Zhu, M. Yan, J. Pan, Y. Yang, W. Deng, J. Lu, X. Huang, and Z. Liu, Phys. Rev. Appl. **16,** 014058 (2021).

[69] Z. G. Chen, W. Tang, R.-Y. Zhang, Z. Chen, and G. Ma, Phys. Rev. Lett. **126,** 054301 (2021).

[70] O. You, S. Liang, B. Xie, W. Gao, W. Ye, J. Zhu, and S. Zhang, Phys. Rev. Lett. **128,** 244302 (2022).

[71] M. Wang, S. Liu, Q. Ma, R. Y. Zhang, D. Wang, Q. Guo, B. Yang, M. Ke, Z. Liu, and C. T. Chan, Phys. Rev. Lett. **128,** 246601 (2022).

[72] J. J. Sakurai and J. Napolitano, *Modern Quantum Mechanics*, 2nd ed. (Addison-Wesley, Boston, 2011).

[73] Y. C. Deng, W. A. Benalcazar, Z. G. Chen, M. Oudich, G. C. Ma, and Y. Jing, Phys. Rev. Lett. **128,** 174301 (2022).

[74] L. Mercadé, K. Pelka, R. Burgwal, A. Xuereb, A. Martínez, and E. Verhagen, Phys. Rev. Lett. **127,** 073601 (2021).

[75] X. L. Dong, P. B. Li, T. Liu, and F. Nori, Phys. Rev. Lett. **126,** 203601 (2021).

[76] M. Landi, J. Zhao, W. E. Prather, Y. Wu, and L. Zhang, Phys. Rev. Lett. **120,** 114301 (2018).